Postprint of: Jha A.K., Lamecki A., Mrozowski M., Bozzi M., A Highly Sensitive Planar Microwave Sensor for Detecting Direction and Angle of Rotation, IEEE Transactions on Microwave Theory and Techniques, vol. 68, no. 4 (2020), pp. 1598-1609, DOI: 10.1109/TMTT.2019.2957369

# A Highly-Sensitive Planar Microwave Sensor For Detecting Direction and Angle of Rotation

Abhishek Kumar Jha, *Member, IEEE*, Adam Lamecki, *Senior Member, IEEE*, Michal Mrozowski, *Fellow, IEEE*, and Maurizio Bozzi, *Fellow, IEEE*

***Abstract*—This paper presents a technique based on a modified complementary split-ring resonator (MCSRR) to detect angular displacement and direction of rotation with high resolution and sensitivity over a wide dynamic range. A detailed comparison of the proposed technique with a few standard CSRR-based sensors shows that the MCSRR is suitable for detecting directional angular rotation with improved sensitivity. The proposed microwave planar sensor takes advantage of the asymmetry of the sensor geometry and measures the angle of rotation in terms of a change in the relative phase of the reflection coefficients. The sensor consists of a movable MCSRR (the rotor) and a microstrip line with a circular hole in the ground plane (the stator). By choosing the substrate material and thickness of the rotor, the sensor can be designed to work at different operating frequencies. A theoretical model of the sensor is proposed, followed by detailed numerical analysis involving equivalent circuit simulations and full-wave computations and measurements. From a positioning error estimation and an air-gap analysis, a technique based on phase-change measurements is found to be better than those based on magnitude measurements alone. An important feature of the proposed technique that even a small anticlockwise or clockwise angular rotation close to the plane of symmetry (such as ± 5°) can be easily detected with high resolution in the relative phase difference of typically around of ± 350°. This property is found to be quite independent of the dielectric loading on the rotor. The maximum sensitivity for measuring the angular rotation is found to be 3.2° change in the relative phase of the reflection coefficient per 1° of rotation. The sensor has an angular measurement range spanning from -90° to 90°. The sensor—a stator fabricated on a 0.5-mm-thick Rogers RT5880 substrate and three rotors fabricated on 1.5-mm-thick Rogers RT5880, 1-mm-thick FR4, and 0.5-mm-thick Rogers RT5880—can effectively detect the direction of rotation and measure the angle of rotation with reasonable accuracy.**

***Index Terms*—Asymmetric devices, directional rotation, angular displacement sensor, electrically small resonators, microwave sensors, microwave measurement technique, rotation sensor.**

Submitted on Aug. 27, 2019.

This work was supported by the Foundation for Polish Science within the TEAM-TECH program, cofinanced by the European Regional Development Fund, Smart Growth Operational Program 2014–2020 (project EDISOn: Electromagnetic Design of flexIble SensOrs).

A. K. Jha and M. Mrozowski are with the Department of Microwave and Antenna Engineering, ETI Faculty, Gdańsk University of Technology, 80-233 Gdańsk, Poland (e-mail: abhishek.jha@pg.edu.pl, mim@pg.edu.pl).

A. Lamecki is with EM Invent, Trzy Lipy 3, 80-172 Gdańsk, Poland (e-mail: adam.lamecki@eminvent.com).

M. Bozzi is with Department of Electrical, Computer and Biomedical Engineering, University of Pavia, 27100 Pavia, Italy (e-mail: maurizio.bozzi@unipv.it).

## I. Introduction

In applications such as space vehicles, the measurement of absolute rotation in space is essential. One way to precisely measure absolute rotation in space is by reference to electromagnetic waves. This method has been employed in designing a microwave-based rotation sensor using the polarization of an electromagnetic wave [1]. A sensor for observing the rate of rotation of a yttrium iron garnet (YIG) film loaded ring resonator in the presence of a biasing magnet was successfully demonstrated in [2], while the magnetoelectric (ME) effect was utilized on a magnetostrictive/piezoelectric laminated composite (MPLC) and a multipole magnetic ring to measure the rotational speed by determining the frequency of the output signal [3]. Recently, two single loop multilayer (SLML) coils employed for wireless power transfer (WPT) were used to detect an angle of rotation in the -40° to 40° range [4]. However, the coil- or magnet-enabled microwave sensors for detecting the angular rotation and velocity are bulky, and usually operate at relatively low frequencies. Of particular interest are planar microwave angular rotation sensors [5]–[13]. A circularly polarized antenna has been proposed for contactless measurement of angular velocity using the ratio of the phase of the transfer function of right-hand (RH) circular polarization and left-hand (LH) circular polarization at 2.5 GHz [5]. Planar structures are particularly suitable for airborne and space applications due to their compact size, lightweight, and easy integration with the monolithic microwave integrated circuit (MMIC) technology. Various kinds of planar resonant designs, coupled with the coplanar waveguide (CPW), have been investigated recently: bisymmetric resonators [6], S-shaped split ring resonators (S-SRR) [7], and electric-LC (ELC) based resonators [8] have been used to measure angular displacement and velocity. A U-shaped resonator was introduced to increase the dynamic range of angular rotation [9] and a horn-shaped SRR was suggested for better linearity [10]. A comb-like nested SRR was proposed for fair linearity in the angular span of 5° [11], while a rotor based on complementary SRR (CSRR) with a microstrip stator module has recently been developed with a sensitivity of 2.37 MHz/° in the dynamic range of 0°–90° [12]. However, it should be noted that most of the planar resonant sensors mentioned above use a symmetric planar transmission line coupled with electrically small resonators, where the angular rotation is measured only by using the absolute value of the transmission coefficient. Due to the symmetry of the sensor design, the

magnitude response of the transmission coefficient is insufficient to provide useful information about the direction of rotation. Such essential parameters often need to be measured precisely for industrial applications and space vehicles. Recently, a planar sensor comprised of a stator and a rotor loaded with circular chains of periodic and aperiodic SRRs was proposed for measuring angular velocity and angular direction, respectively [13]. The technique used there involves frequency division multiplexing of an amplitude-modulated signal with two carrier frequencies, which requires a diplexer, combiner, and additional digital processing toolkits. The overall size of the sensing unit is at least over twice the operating wavelength; the technique is not straightforward and is based on amplitude measurement alone.

This paper presents a novel technique for detecting and measuring angular direction and angular rotation, exploiting the asymmetric properties of the microstrip-coupled modified complementary SRR (MCSRR) sensor. The proposed planar sensor also measures the angular rotation in a wide dynamic range and, when equipped with various rotors, can operate at different frequencies. Moreover, the design is rather immune to positioning errors and to the height of the air gap between the stator and the rotor. The angular rotation is measured in terms of the relative change in the phase of reflection coefficients, which varies substantially due to changes in cross-coupling between the microstrip line and the MCSRR-based rotor. A theoretical explanation with an equivalent two-port network model is derived and verified using the results obtained from the circuital and numerical analysis. The sensor is quite sensitive to angular direction and angular rotation, while the overall size of the sensor is less than half of the operating wavelength.

This paper is organized as follows: Section II discusses the general theory of CSRR-based asymmetric sensors that detect and measure angular direction and rotation using the phase of the scattering parameters. Based on the theory developed in section II, a new CSRR structure that increases the sensitivity over that of earlier structures is proposed in Section III. Section IV deals with various issues of pragmatic sensor design and their solutions in the proposed scheme. Measurements and results are provided in section V, while section VI concludes the paper.

## II. Circuit and Full-Wave Analysis of a DCSRR-based Sensors

The sensor proposed here is a modified version of that described in [12]. To understand how that sensor should be modified to detect the direction of rotation with good sensitivity over a wide span of angular rotation, the properties of the original structure need to first be presented. A detailed sketch of the sensor is presented in Figure 1(a). The sensor consists of a microstrip line with a circular opening etched out in the ground plane. The double CSRR (a rotor) is assumed to be placed over the etched opening and is allowed to rotate without any physical contact with the ground of the microstrip line. The angular span of the double CSRR (DCSRR) is assumed to be from -90° to 90° in the anticlockwise and clockwise directions, as shown in Figure 1(b). The construction of the rotor, the DCRSS, and the geometric parameters are presented in Figure 1(c). The planar sensor can be described by the equivalent circuit shown in Figure 1(d), which considers the cross-coupling effects arising due to the electric and magnetic coupling when $\theta \neq 0°$ [14]. As shown in [12], the magnetic coupling depends on the rotation angle, and since the resonant frequency is a function of mutual coupling $M$, the angle can be determined quite accurately by measuring the resonant frequency of the sensor. Since the resonant frequency is an even function of the angle, the sensor developed in [12] cannot distinguish the sense of rotation. Note, however, that the cross-coupling effect induces asymmetry in the two-port network shown in Figure 1(d), which is accounted for in an equivalent T-network given in Figure 1(e) where the series impedances, i.e. $Z_1$ and $Z_2$ are unequal.

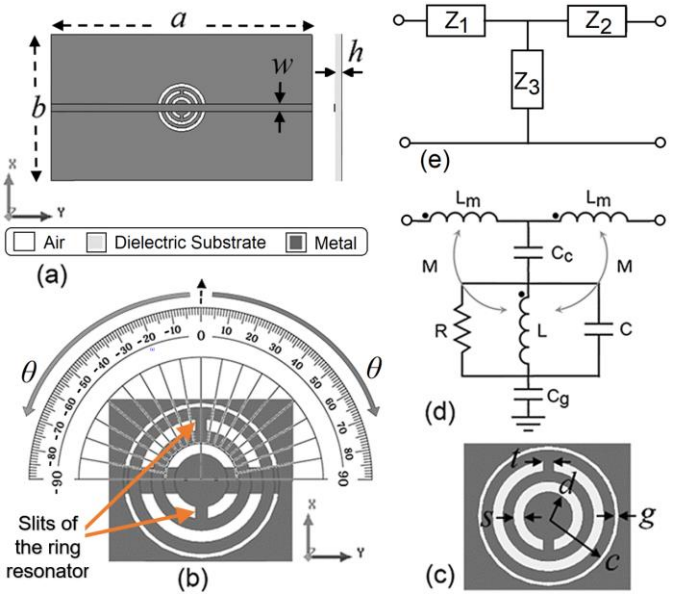


Figure 1. (*a*) top view of the planar sensor proposed in [7] (with transparent substrate), (*b*) angular rotation dynamics of the rotor, (*c*) enlarged view of the DCSRR with details of design parameters, (*d*) the equivalent lumped element circuit representation of the design, and (*e*) the equivalent T-matrix representation of the proposed sensor.

Considering the current flowing in the circuit and the dot convention of the inductor, the impedances of the T-section can be given as

$$Z_1 = j\omega(L_m - M); \quad Z_2 = j\omega(L_m + M)$$
$$Z_3 = \frac{\omega^2 L'^2 R}{R^2(\omega^2 L'C-1)-\omega^2 L'^2} + j\left\{\frac{\omega L' R^2(\omega^2 L'C-1)}{R^2(\omega^2 L'C-1)-\omega^2 L'^2} - \frac{C_c + C_g}{\omega C_c C_g}\right\} \quad (1)$$

where $L'$ is the effective inductance of the RLC network subjected to cross-coupling, and can be given as $L$-2$M$. When matched with the characteristic impedance of the source $Z_0$, the two-port scattering parameters of the T-network can be written as

MOST WIEDZY Downloaded from mostwiedzy.pl

$$S_{11} = \frac{Z_0(Z_1 - Z_2) + \sum_{i \neq j} Z_i Z_j - Z_0^2}{Z_0 \sum_{i=1} Z_i + \sum_{i \neq j} Z_i Z_j + Z_0 Z_3 + Z_0^2} \quad (2)$$

$$S_{22} = \frac{Z_0(Z_2 - Z_1) + \sum_{i \neq j} Z_i Z_j - Z_0^2}{Z_0 \sum_{i=1} Z_i + \sum_{i \neq j} Z_i Z_j + Z_0 Z_3 + Z_0^2}$$

$$S_{21} = S_{12} = \frac{Z_0 Z_3}{Z_0 \sum_{i=1} Z_i + \sum_{i \neq j} Z_i Z_j + Z_0 Z_3 + Z_0^2}. \quad (3)$$

From (1)–(3), it can be observed that the sensor is reciprocal but asymmetric under angular rotation ($\theta \neq 0°$). This asymmetry can be used to detect the rotation direction. To illustrate this, we consider the response of the equivalent circuit, assuming that the stator and rotor are fabricated on a 0.508-mm-thick Rogers RT5880 substrate (of dielectric constant 2.2 and loss tangent 0.0009) with copper thickness 18 µm; the sensor is designed to operate at the industrial, scientific, and medical (ISM) radio frequency band centered at 5.8 GHz.

### *A. Extraction of Circuit Parameters*

First of all, the full-wave electromagnetic solver is used to model the DCSRR, as shown in Figure 1(a), and the two-port scattering parameters (S-parameters) are calculated. To avoid the complexity of developing a mathematical model that includes the cross-coupling effect, the symmetric case with $\theta = 0°$ is preferred, and the initial circuit parameters are obtained as in [15]. In the next step, the initial values of the circuit parameters for $\theta = 0°$ are used to model the circuit of Figure 1(d) into the circuit simulator ADS. A small tuning of circuit parameters in ADS provides a good match for the S-parameters calculated using the full-wave solver. The values of the circuit elements are fixed; the mutual coupling for $\theta \neq 0°$ is now considered using the mutual inductor component of ADS, and the value of $M$ is extracted. In this process, a parametric simulation with respect to $\theta$ (-90° to -90°) is carried out in the full-wave solver and the S-parameter data are imported to ADS. The mutual coupling $M = k\sqrt{LL_m}$ is calculated for each value $\theta$ whenever a good match between the simulated and calculated S-parameters is observed by adjusting the mutual coupling coefficient, $-1 \leq k \leq 1$. The final values of the circuit parameters, along with the design parameters of the sensor shown in Figure 1, are given in Table I.

TABLE I. DESIGN PARAMETERS AND THEIR VALUES

| Parameters | Value (mm) | Parameters | Value |
|---|---|---|---|
| $a$ | 40 | $C$ | 1.78 pF |
| $b$ | 25 | $C_c$ | 0.3 pF |
| $c$ | 3.5 | $C_g$ | 0.6 pF |
| $d$ | 1.5 | $L$ | 0.39 nH |
| $g$ | 0.5 | $L_m$ | 3.8 nH |
| $h$ | 0.508 | $R$ | 3 kΩ |
| $s$ | 0.5 | $M$ | ± 0.12 nH |
| $t$ | 0.5 | $f$ (0°), $f$ (± 90°) | 5.73 GHz, 5.88 GHz |
| $w$ | 1.49 | $Q$ | 231–225 |

For the parameters given in Table I, the magnitude and phase response of the two-port scattering parameters of the sensor have been calculated using numerical and circuital methods. For this analysis, the DCSRR has been assumed to rotate from -90° to 90° with a step of $\theta = 45°$; the results are presented in Figure 2.

From Figure 2, it can be observed that the magnitude and phase response of the two-port sensor evaluated using numerical and circuit analysis are in good agreement. It is very clear from Figure 2 that the magnitude response of the scattering coefficients could not differentiate angular rotation between $\theta$ = -90° and 90° or between $\theta$ = -45° and 45°. However, the phase response of the DCSRR-based sensor, which is symmetrical and reciprocal only at $\theta = 0°$, is different for positive and negative rotation angles. It can be seen from the phase profiles of the scattering coefficients of the two-port network that the phase of $S_{21}$ and $S_{12}$ remains nearly unchanged, while the phase of $S_{11}$ and $S_{22}$ are quite sensitive to the directional rotation. This property can thus be instrumental in effectively detecting and measuring the directional angular rotation.

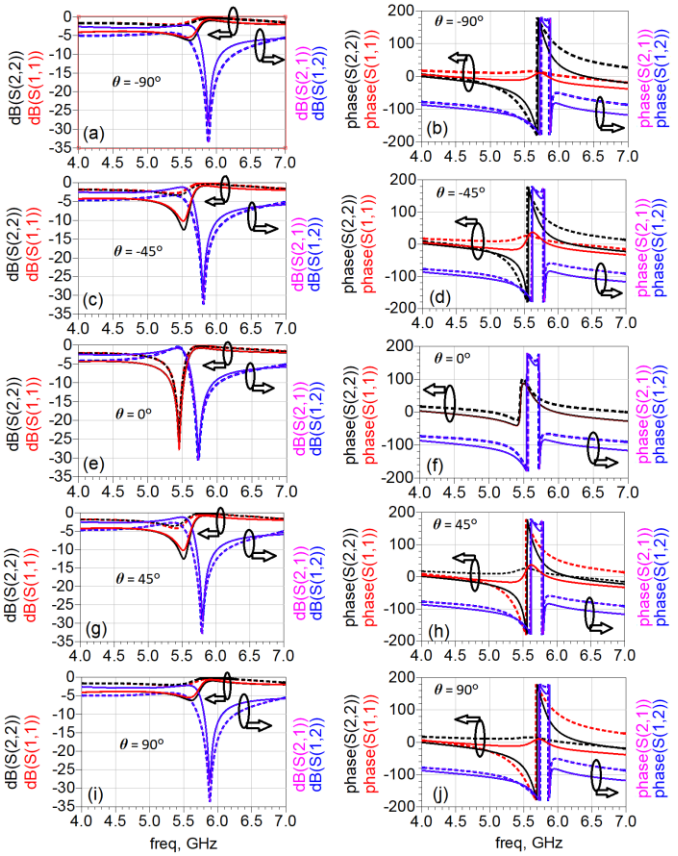


Figure 2. Simulated and calculated values of magnitude and phase of scattering coefficients of the sensor under rotation; mutual coupling with respect to the angle of rotation k = ± 0.16, 0, and ± 0.23 for $\theta$ = ± 45°, 0°, and ± 90°, respectively. [Solid lines: Numerical simulation, Dashed lines: Circuit analysis]

The analysis of the frequency response of the DCSRR-based sensor suggests that measurement of directional rotation should be based on the asymmetric behavior of the phase of $S_{11}$ and $S_{22}$. From Figure 1, it can be noted that the slits in the DCSRR, when not at $\theta = 0^0$, introduce asymmetry into the two-port network. The asymmetric behavior is observed due to the change in the magnetic flux of the microstrip line crossing the DCSRR slits, which alters the amount of magnetic coupling when rotated either clockwise or anticlockwise.

MOST WIEDZY Downloaded from mostwiedzy.pl

## III. Modified Structure with Improved Sensitivity

The asymmetric phase response presented in section II is essentially due to the cross-coupling effect produced by both the CSRR slits. To enhance the cross-coupling effect, and hence the sensitivity, it would seem to be beneficial to modify the resonating structure. To find a suitable geometry for the rotor, we consider two single-slit CSRR configurations: The first one involves a single CSRR, rather than a DCSRR, as shown in Figure 3(a). In the second configuration, a rotor is based on a modified CSRR (MCSRR), from which the upper part of the central circular patch has been removed, as shown in Figure 3(b). The length of the slit is increased from *s* to *d* while keeping the thickness *t* the same. The removal of the upper part increases the amount of magnetic flux linkage of the microstrip line. The mechanism behind this is explained below.

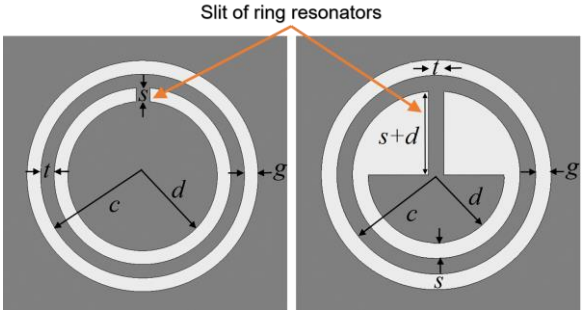


(a) (b)

Figure 3. (*a*) Standard CSRR structure and (*b*) proposed MCSRR structure for enhanced magnetic coupling

The MCSRR structure with the enhanced cross-coupling effect is derived by considering the magnitude and direction of the surface current at the resonating frequency in the DCSRR and CSRR, as shown in Figure 4. For simplicity, two angular configurations are considered: Figure 4(a)–(f) shows the surface currents on the rotor for $\theta$ = 0°, while Figure 4(g)–(l) corresponds to $\theta$ = -90° (the results for $\theta$ = 90° can be obtained from Figure 4(g)–(l) by considering the mirror image in the *y* = 0 plane). Figure 4(a)–(c) shows the magnitude of the surface current, while Figure 4(d)–(f) show the direction of the surface current of the DCSRR, CSRR, and MCSRR, respectively, stationed at $\theta$ = 0°. At $\theta$ = 0°, the surface current is symmetric across the ports of the sensor and therefore does not induce any cross-coupling effect. However, the magnitude and direction of the surface current shown in Figure 4(g)–(i) and Figure 4(j)–(k) demonstrate that the surface current is not symmetric across the ports of the sensor for $\theta$ = -90°. On close observation, it can be seen that current flowing into the two slits of the DCSRR are antiparallel and unequal in magnitude; if the net current flowing in the outer slit is $J_1$ and that in the inner slit is $J_2$ (with $J_1 > J_2$), the net current flowing in DCSRR of $J_1$-$J_2$ would always be less than the current flowing in CSRR, $J_1$, due to the single slit having the same dimension. Consequently, the magnetic flux responsible for cross-coupling is larger in CSRR than in DCSSR. The cross-coupling effect can be enhanced through increased magnetic flux linkage by using the slit of the ring resonators. This is achieved by modifying the geometry of CSRR and increasing the slit length, by etching the metal around the slit while keeping the other dimensions fixed. The effect of modification in the slit can be observed from the surface current distribution of MCSRR at $\theta$ = -90°, which shows the current passing through the modified slit ($J_3 > J_1$). The overall cross-coupling phenomenon can be summarized by comparing the net current in DCSRR, CSRR, and MCSRR (Figure 4), and can be given as $J_{DCSRR} < J_{CSRR} < J_{MCSRR}$.

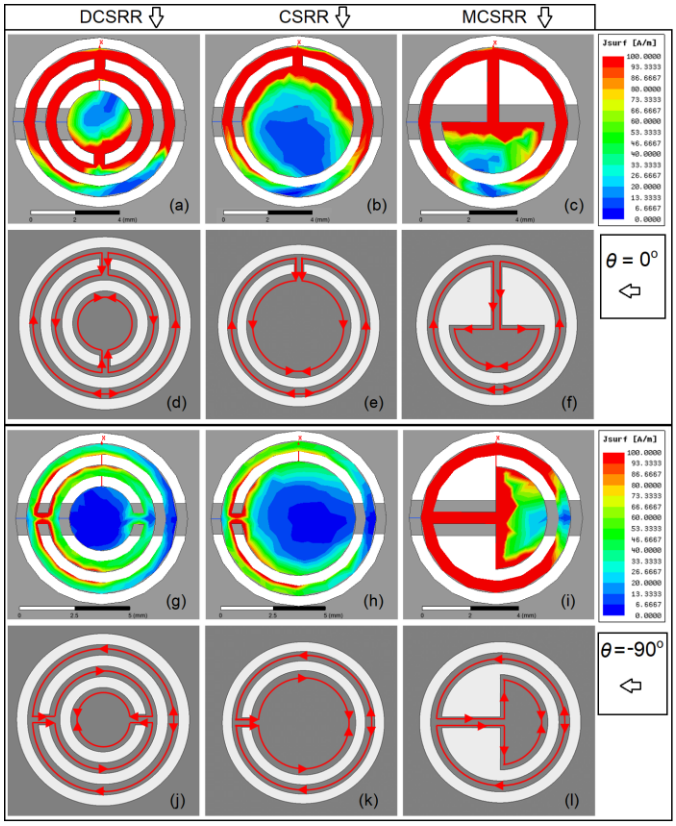


Figure 4. Magnitude plots of (*a*) DCSRR, (*b*) CSRR, and (*c*) MCSRR; vector plots of (*d*) DCSRR, (*e*) CSRR, and (*f*) MCSRR at $\theta$ = 0°; magnitude plots of (*g*) DCSRR, (*h*) CSRR, and (*i*) MCSRR; vector plots of (*j*) DCSRR, (*k*) CSRR, and (*l*) MCSRR at $\theta$ = -90° (fixed dimensions are *c* = 3.5 mm, *g* = *s* = *t* = 0.5 mm).

After explaining the cross-coupling effect by means of surface current distribution, a detailed numerical analysis was performed to observe the characteristics of the CSRR and MCSRR; the results were compared to the response of DCSRR in terms of the calculated resonant frequency *f*, the loaded quality factor *Q*, and the phase of $S_{11}$ and $S_{22}$ of the DCSRR, CSRR, and MCSRR. To obtain better understanding, the DCSRR, CSRR, and MCSRR were compared for a fixed value of *c* = 3.5 mm; the results are shown in Figure 5, where the values of *f* and *Q* of the CSRR and MCSRR are normalized with respect to the resonant frequency and the loaded quality factor of the DCSRR at 0°, which were found to be 5.73 GHz and 225, respectively. It is quite difficult to analyze the exact circuit parameters of CSRR and MCSRR in comparison with DCSRR; however, the change in circuit parameters can be explained from the response of *f* and *Q*, as given in Figure 5(a) and (b), respectively. The rotor circuit from the DCSRR (Figure 1(c)) to CSRR (Figure 3(a)) and MCSRR (Figure 3(b))—each of which has the same unit cell size (*c* = 3.5 mm) and is coupled through same the microstrip line and gap from ground, *g*—can be considered with a

MOST WIEDZY Downloaded from mostwiedzy.pl

constant electric coupling: the values of $C_c$ and $C_g$ are fixed. The presence of one ring in the CSRR significantly reduces the value of $C$ compared to DCSRR, while increasing the effective value of $L$ ($L_{eff}$) due to the presence of a single slit when $\theta \neq 0°$. The effect of the change in the values of the circuit for CSRR can be seen from the increase in the resonant frequency (that is, $f \propto C^{-0.5}$) and the decrease in $Q$ ($Q \propto C$), as shown in Figures 5(a) and 4(b), respectively. Since the change in $Q$ of the CSRR is inversely proportional to the change in $L_{eff}$ ($\Delta Q \propto \Delta L_{eff}^{-1}$), which is always greater than the resultant $L_{eff}$ of DCSRR—where the two slits are placed antiparallel—a significant increase in the dynamic range of $Q$ for CSRR is observed in Figure 5(b). It is quite interesting to note that the loaded quality factor of DCSRR, which varied from 225 ($\theta$ = 0°) to 231 ($\theta$ = ± 90°), so that $\Delta Q$ = 6, is now found to vary from 168 ($\theta$ = 0°) to 248 ($\theta$ = ± 90°) for the CSRR; now $\Delta Q$ = 80. This increased dynamic range of $Q$ with respect to $\theta$ is mainly due to the noticeable asymmetry in the CSRR (single slit), unlike in the DCSRR (double slit). In order to increase the asymmetry even further, a modified rotor design (MCSSR) was analyzed and compared with the DCSRR and CSRR. In the MCSRR, the extended etching increases $C$ when compared with CSRR, while a longer slit ($\Delta$ = $d$-$s$) increases $L$ at the same time. The higher values of $L$ and $C$ in the MCSRR than in the CSRR significantly decrease the value of $f$. The resonant frequency of DCSRR was found to be the arithmetic mean of $f_{CSRR}$ and $f_{MCSRR}$ at $\theta$ = 0°, as can be seen in Figure 5(a). Figure 5(b) shows that the normalized $Q$ of MCSRR is greater than the normalized $Q$ of CSRR, suggesting a significant increase in the value of $L$, as compared to $C$ of MCSRR at $\theta$ = 0°. The modified $L$ in MCSRR is the key point for enhancing asymmetry in cross-coupling at $\theta \neq 0°$, which is essential for detecting and measuring the directional rotation.

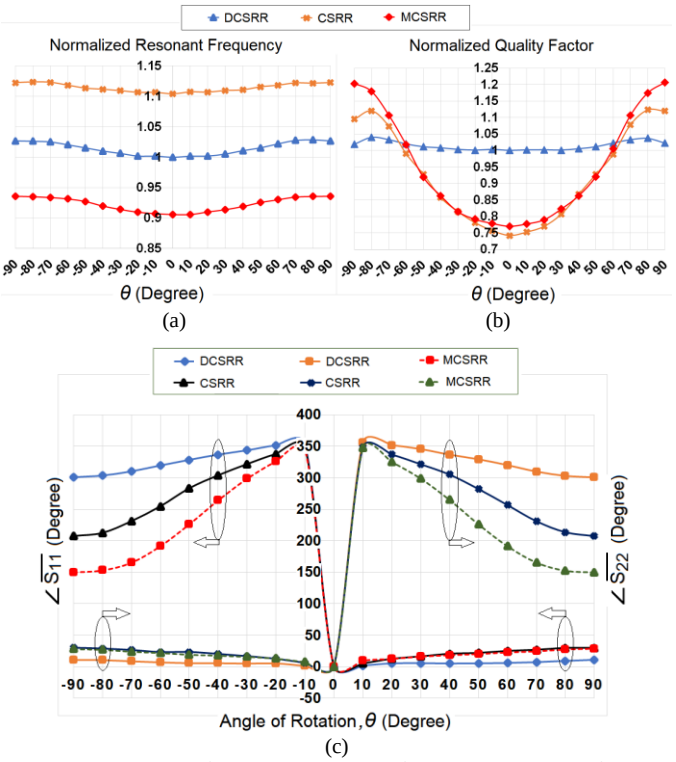


Figure 5. (*a*) Resonant frequency, (*b*) quality factor, and (c) phase of $S_{11}$ and $S_{22}$ of the CSRR, DCSRR, and MCSRR

As noted, and as can be observed from Figure 5(a) and (b), the value of $f$ and $Q$, whether alone or together, cannot provide information on directional rotation. Both are even functions of the rotation angle. However, the angle's value and the sign can be calculated from the phase of $S_{11}$ and $S_{22}$, as shown in Figure 5(c). From this figure, it can be observed that each of the rotor circuits—DCSRR, CSRR, and MCSRR—provide an indication of the sense of rotation in terms of the change in phase of the reflection coefficient at port 1 or port 2, respectively. In this figure, the phase of $S_{11}$ and $S_{22}$ of each rotor is normalized with respect to the phase of $S_{11}$ and $S_{22}$ of the individual rotors at $\theta$ = 0°. The sensitivity of the measurements can be defined as the slope of curves in Figure 5(c):

$$S^{-} = \frac{\Delta\angle\overline{S_{11}}}{\Delta\theta} = \frac{\Delta\left(\angle S_{11} - \angle S_{11}|_{\theta=0°}\right)}{\Delta\theta}, \qquad S^{+} = \frac{\Delta\angle\overline{S_{22}}}{\Delta\theta} = \frac{\Delta\left(\angle S_{22} - \angle S_{22}|_{\theta=0°}\right)}{\Delta\theta} \tag{4}$$

where $S^{-}$ and $S^{+}$ are the anticlockwise and clockwise sensitivities. From Figure 5(c), it is evident that the sensitivity increases with the asymmetry of the rotor, in the sequence DCSRR < CSRR < MCSRR. It can be seen from Figure 5(c) that, for anticlockwise rotation (-90° ≤ $\theta$ < 0°), the value of $\angle\overline{S_{11}} > \angle\overline{S_{22}}$, so that $S^{-} > S^{+}$; the converse is also true. It can thus be concluded that the directional angular rotation can best be measured with enhanced sensitivity using the proposed MCSRR-based rotor, coupled with the microstrip line-based stator. It is worth mentioning here that Figure 5(c) shows how the phase is very asymmetric, unlike the amplitude, which is an even function of the angle. A large phase swing can be seen when the rotor rotates clockwise or anticlockwise from its initial position ($\theta$ = 0°), and was found to be almost same for all rotors (~350°). Because of this, the phase measurement-based scheme is expected to be much more sensitive at detecting the angular rotation than the magnitude-based rotation sensing technique.

## IV. Practical Realization

Prior to fabrication of the proposed sensor, involving a microstrip line-based stator and an MCSRR-based rotor, the design was tested via a series of numerical simulations to considering practical limitations, for which feasible solutions are also provided in this section. The four major issues—practical fabrication of the rotor, accurate phase measurement, positioning error of the rotor, and the air gap between the stator and the rotor—were numerically studied to find practical solutions.

### *A. Realization of the Rotor*

The rotor discussed above was not considered as a separate block; however, a rotor in practice must be free to rotate around its axis. The rotor thus needs to be fabricated on a separate substrate. This provides an additional degree of freedom in choosing the dielectric constant and the height of the rotor. A number of MCSRR-based rotors were analyzed by altering the dielectric constant $\varepsilon_r$, and the height $h_r$ of the substrate, as shown in the inset to Figure 6(a); the resonant

MOST WIEDZY Downloaded from mostwiedzy.pl

frequency $f$, the loaded quality factor $Q$ at $\theta$ = 0°, and the bandwidth of rotation $\Delta f$, and the change in the quality factor $\Delta Q$ due to the rotation from $\theta$ = 0° to ± 90° are all provided in Figure 6.

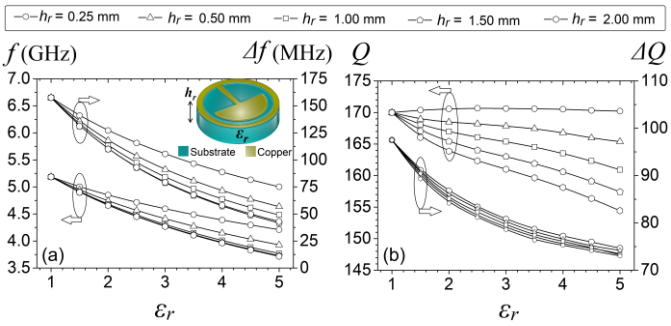


Figure 6. (*a*) Resonant frequency and bandwidth; (*b*) quality factor and change in quality factor of various MCSRRs with $\varepsilon_r$ ranging from 1 to 5, $h_r$ ranging from 0.25 to 2, and $\theta$ ranging from 0° to ± 90°

A number of observations can be made from Figure 6: First, the freedom to choose the $\varepsilon_r$ and $h_r$ of the rotor independently from the stator makes it possible to select the operating frequency within a wideband: for example, dielectric loadings of $\varepsilon_r$ = 2, 3, 4 and 5 give operating bands in the range of 5.19 GHz to 4.21 GHz, 3.93 GHz, 3.77 GHz, and 3.72 GHz for $h_r$ = 0.25 mm, 0.5 mm, 1 mm, and 1.5 mm respectively. Second, an increase in $h_r$ beyond 1.5 mm shows almost no effect on the response of the dielectric loading, due to the confinement of the near field in the close vicinity of the ground plane. Third, lower values of $h_r$ and $\varepsilon_r$ provide better angular bandwidth of magnitude-based measurement (i.e., $\Delta f$ and $\Delta Q$) than for $\varepsilon_r$ = 5 and $h_r$ = 2 mm. Fourth, the dielectric loading in terms of increased $h_r$ or $\varepsilon_r$ slightly reduces the value of $Q$, where a higher value of $\varepsilon_r$ reduces $\Delta Q$ than does $h_r$. The pronounced effect of $h_r$ on the absolute value of $Q$, despite its almost trivial effect on $\Delta Q$, can be understood by the fact that, for a given $\varepsilon_r$ and $h_r$, $\Delta Q$ is mainly dependent on the mutual inductive coupling between the microstrip line (on the stator) and the slit of the MCSRR (on the rotor).

### *B. Relative Phase Measurement and Sensitivity*

The asymmetric phase of the reflection coefficients of the MCSRR-based two-port sensor is the essential element in detecting and measuring the directional rotation with improved sensitivity. However, the absolute phase measurement of the microstrip-based sensor—which may vary significantly with even a small shift in the reference plane—does not seem to represent a very practical approach for measuring angular rotation. It is thus the relative change in the phases of $S_{11}$ and $S_{22}$ at a moment of rotation $\phi$ that can be used to calculate the sensitivity of the sensor, thus:

$$S = \left|\frac{\Delta\phi}{\Delta\theta}\right| = \left|\frac{\Delta\left(\angle S_{11} - \angle S_{22}\right)}{\Delta\theta}\right| \tag{5}$$

To measure the angular rotation, estimation of $\phi$ is more convenient than calculating the two expressions $\angle\overline{S_{11}}$ and $\angle\overline{S_{22}}$ using (4), which would involve absolute phase measurement. Moreover, the relative phase measured using (5) has a negative value for anticlockwise rotation and a positive value for clockwise rotation. Phase measurement-based sensors are thus more distinctive, which may open up more opportunities for a designer than magnitude-based schemes. A number of rotors with various values of $\varepsilon_r$ (= 2, 3, 4, and 5) and $h_r$ (= 0.25 mm, 0.5 mm, 1 mm, and 1.50 mm) were considered to calculate $\phi$ using (5), and the results are shown in Figure 7.

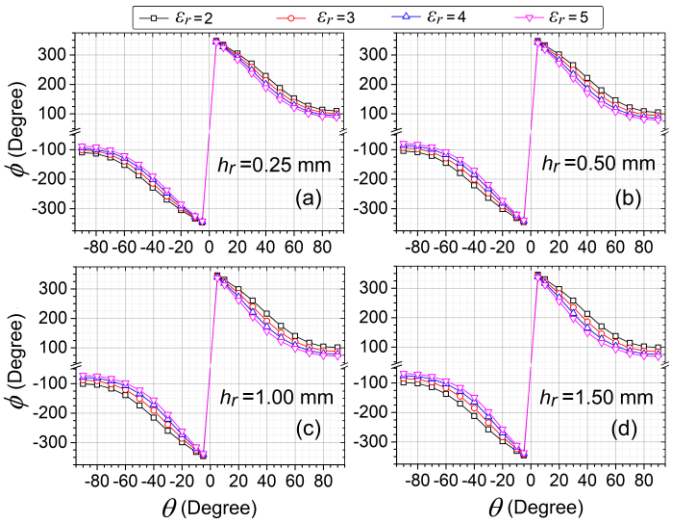


Figure 7. Relative phase of $S_{11}$ and $S_{22}$ calculated for various rotors with $\varepsilon_r$ = 2 to 5 and $h_r$ = (*a*) 0.25 mm, (*b*) 0.50 mm (*c*) 1.0 mm, and (*d*) 1.50 mm, while $\theta$ ranged from 0° to ± 90°

From Figure 7, it can be seen that dielectric loading on the rotor, in the form of increments in the values of $\varepsilon_r$, and $h_r$, slightly increases the sensitivity of the sensor. It is interesting to see that dielectric loading improves the sensitivity of the sensor, if only slightly. On the other hand, the sensitivity calculated using the magnitude response always decreases with increased dielectric loading, as can be seen from Figure 6 (i.e., the response of $\Delta f$ and $\Delta Q$). Figure 7 shows that the sensitivity can be arranged in increasing order as $(S_{hr\,=\,0.25\text{mm}} < S_{hr\,=\,0.5\text{mm}})_{\varepsilon r\,=\,2} < (S_{hr\,=\,1\text{mm}})_{\varepsilon r\,=\,2} \approx (S_{h\,=\,0.25\text{mm}})_{\varepsilon r\,=\,3} < (S_{hr\,=\,1.5\text{mm}})_{\varepsilon r\,=\,2} < (S_{hr\,=\,0.5\text{mm}})_{\varepsilon r\,=\,3} \approx (S_{h\,=\,0.25\text{mm}})_{\varepsilon r\,=\,4} < (S_{hr\,=\,1\text{mm}})_{\varepsilon r\,=\,3} \approx (S_{h\,=\,0.25\text{mm}})_{\varepsilon r\,=\,5} < (S_{hr\,=\,1.5\text{mm}})_{\varepsilon r\,=\,3} \approx (S_{h\,=\,0.5\text{mm}})_{\varepsilon r\,=\,4} < (S_{hr\,=\,1\text{mm}})_{\varepsilon r\,=\,4} \approx (S_{h\,=\,0.5\text{mm}})_{\varepsilon r\,=\,5} < (S_{hr\,=\,1.5\text{mm}})_{\varepsilon r\,=\,4} < (S_{hr\,=\,1\text{mm}} < S_{hr\,=\,1.5\text{mm}})_{\varepsilon r\,=\,5}$. The minimum and maximum values of the average sensitivity calculated from (5) were found to be respectively 2.8 and 3.2, expressed as the relative phase of reflection coefficient in degrees per rotational degree.

We note here that the response of $\phi$ with respect to $\theta$ for various dielectric loadings in Figure 7 also changes the frequency of operation, which is quite advantageous for the selection of band of operation. Among various possible combinations of the MCSRR-based rotors, the frequency response of two limiting dielectric loadings—rotor1 with $\varepsilon_r$ = 2 and $h_r$ = 0.25 mm and rotor2 with $\varepsilon_r$ = 5 and $h_r$ = 1.50 mm—are shown in Figure 8. These two rotors were chosen to show that the selection range of frequency and quality factor provided by dielectric loading lie in the ranges of $f$ = 3.77 GHz to 4.85 GHz, $Q$ = 157 to 171, with $\Delta f$ = 43 MHz to 127 MHz and $\Delta Q$ = 72 to 87, as can be seen from Figure 6. Comparing Figure 8(a) and (b) with Figure 8(c) and (d), respectively, it can be observed that our approach has two significant advantages: *i*) the loading on rotor, even though it selects the frequency of operation and the bandwidth, does not negatively

MOST WIEDZY Downloaded from mostwiedzy.pl

affect the sensitivity, but in fact improves it, and *ii*) extreme sensitivity to the direction of angular rotation, when the rotor starts from stationary position ($\theta$ = 0°). We can note from Figures 7 and 8 that our scheme provides very high resolution in detecting anticlockwise and clockwise rotation beginning from $\theta$ = 0°. This can be understood by noting that a small angular rotation of MCSRR-based rotor from $\theta$ = 0° to ± 5° can be easily detected by a substantial change in the value of $\Delta\phi$, typically from 0° to ± 350°. In other words, the sensitivity of the proposed technique for detecting small angular rotation near to the symmetrical axis is quite high at 70 °/°.

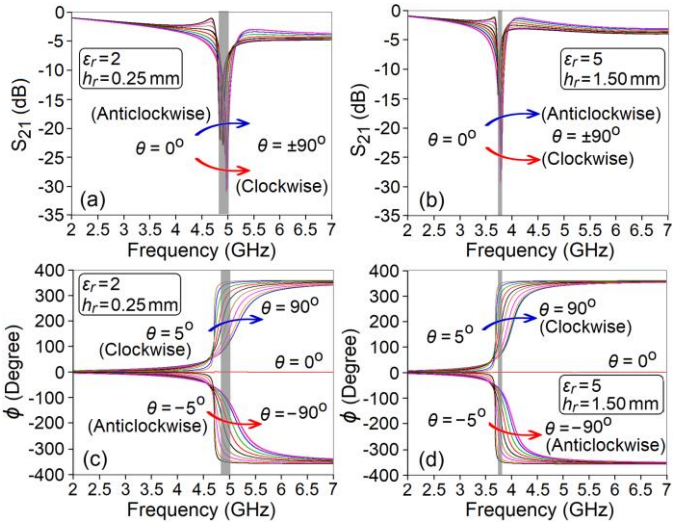


Figure 8. Frequency response of the magnitude of $S_{21}$ for (*a*) rotor1 and (*b*) rotor2; relative phase for (*c*) rotor1 and (*d*) rotor2 with respect to $\theta$.

### C. *Positioning Error Estimation*

As can be seen from Figure 3(b), a gap of width $g$ = 0.5 mm was engraved between the ground plane and the MCSRR to facilitate the free rotation of the rotor around its axis. In practice this gap could introduce a positioning error due to the misalignment of the axis of rotation with the geometric center, or due to a mechanical or manual error in placing the rotor on the stator. The positioning error is thus calculated as the relative phase $\phi$(x, y) at a given coordinate normalized with respect to $\phi$(0, 0). For estimating the error in $\phi$ due to a misaligned rotor, a tolerable mechanical or manual error of 100 µm was considered for both the x and y directions, as shown in Figure 1(a), where the origin is taken as the geometric center of the stator. The positioning error in $\phi$ for a particular angle of rotation can be given as:

$$\left(\overline{\Delta\phi_p}\right)_\theta = \left[(\phi)_{(x,y)} - (\phi)_{(0,0)}\right]_\theta \tag{6}$$

The positioning errors in $\phi$ for each of the rotors with various combinations of dielectric constant $\varepsilon_r$, height $h_r$, and angle of rotation $\theta$ were compared using (6). As before, we consider two dielectric loading cases, rotor1 and rotor2. The positioning errors for these MCSRR-based rotors with two dielectric loading conditions were calculated for various angular positions, and the results for three particular cases ($\theta$ = -90°, 0°, and 90°) are given in Figure 9.

Contour plots of the error in $\phi$ for the rotors with $\varepsilon_r$ = 2 (and 5), $h_r$ = 0.25 mm (and 1.5 mm) are provided for $\theta$ = -90°, 0°, 90° in Figure 9(a), (b), (c) (and Figure 9(d), (e), (f)), respectively. The relative phase in the initial state, $\phi$(0, 0) for the configurations shown in Figure 9(a), (b), (c) and Figure 9(d), (e), (f) are calculated as 111°, 0°, -110° and 60°, 0°, -60° for the angular rotations $\theta$ = -90°, 0°, 90°, respectively. It is interesting to note from Figure 9 that the error in $\phi$ is mainly observed for the positioning error of the rotor along the y-axis, while it is found to be nearly independent of the displacement along the x-axis. This can be understood by considering that the relative phase measurement for a transmission line of given length at a fixed reference plane is nearly constant, while it varies with the change in the reference plane along the direction of propagation (the y-axis). A close comparison of Figure 9(a) with (c) (and Figure 9(d) with (f)) shows that the values of $\overline{\Delta\phi_p}$ for $\theta$ = -90° and $\theta$ = 90° are mirrored and are each other's negative along the y-axis. Also, for low dielectric loading on the rotor, the positioning error for $\theta$ = 0° (the symmetrical condition) is less than that for $\theta$ = ± 90° (the asymmetrical condition). Another interesting fact that can be noted from Figure 9 is the reduction in the positioning error due to the increase in dielectric material loading on the rotor. Combining the results from Figures 7 and 9, we can see that the dielectric loading not only increases the sensitivity but also reduces the positioning error.

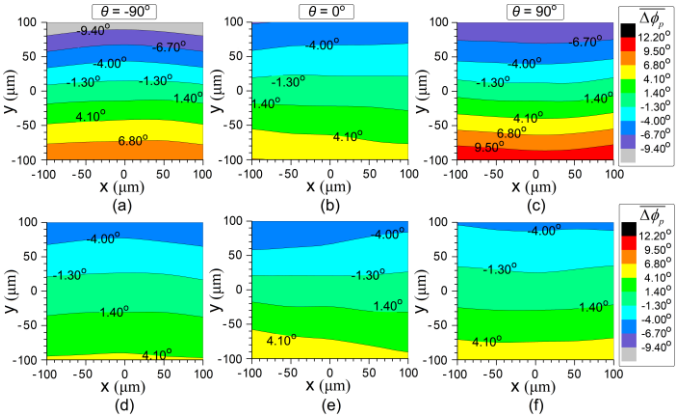


Figure 9. Positioning error for rotor1 with angular position (*a*) $\theta$ = -90°, (*b*) $\theta$ = 0°, (*c*) $\theta$ = 90°; and for rotor2 with angular position (*d*) $\theta$ = -90°, (*e*) $\theta$ = 0°, and (*f*) $\theta$ = 90°.

TABLE II. MAXIMUM POSITIONING ERROR AND RANGE OF MEASUREMENT FOR VARIOUS PARAMETERS

| Parameters | Max. positioning error for (Δx, Δy) = (± 100 µm, ± 100 µm) | | | Dynamic Range | Max. % Error |
|---|---|---|---|---|---|
| | $\theta$ = -90° | $\theta$ = 0° | $\theta$ = 90° | | |
| $\phi$ (degree) | ± 5.9 | ± 6.9 | ± 6.1 | ± 269 | ± 2.6 |
| $f_r$ (MHz) | 9 | 21 | 6 | 42 | 50 |
| $Q$ | 8 | 3 | 7 | 74 | 11 |

Table II quantitatively compares the maximum positioning error in the measurable parameters with respect to their range of measurement, the error in relative phase, the resonant frequency, and the quality factor for the MCSRR-based rotor2. From this, it can be seen that our scheme not only provides better sensitivity and directional rotation over a wide dynamic range, but also offers smaller positioning errors than the other measurable parameters.

MOST WIEDZY Downloaded from mostwiedzy.pl

### D. Air Gap Analysis

In this design, the rotor is considered a separate block that not only provides useful features (such as selection of the operating band, choice of material, and height of the rotor) but also makes the design practical. However, since the stator and the rotor are separate, an air gap exists between them. To determine the impact of this air gap, a numerical analysis of the error in relative phase was carried out, assuming that the gap between the stator and the rotor changes from z = 0 to 100 µm. The error in the relative phase with respect to the angle of rotation can be given as:

$$\left(\overline{\Delta\phi_{ag}}\right)_{\theta} = \left[(\phi)_z - (\phi)_{(z=0)}\right]_{\theta} \tag{7}$$

Again, the two rotors (rotor1 and rotor2) have been considered in obtaining the range of $\overline{\Delta\phi_{ag}}$ with respect to $\theta$. The medium between the stator and the rotor is modeled as air in the full-wave electromagnetic solver. The magnitude and phase of the scattering parameters were calculated around the resonant frequency of the sensor with an air gap, whereas the value of the error in the relative phase was evaluated using (7) and plotted in Figure 10 for $\theta$ = 0° and ± 90°.

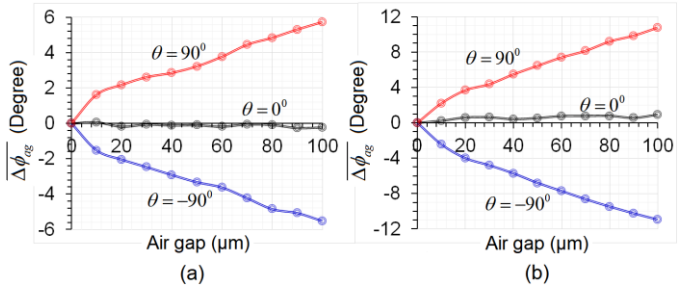


Figure 10. Error in relative phase measurement due to the presence of an air gap between the stator and (*a*) rotor1 and (*b*) rotor2.

From Figure 10(a) and (b), we can see that rotor2 with the air gap experiences a higher error in the relative phase than rotor1 due to the increased dielectric material loading. It is worth mentioning that the errors in the relative phase for rotor1 and rotor2 with the air gap are lower than the errors calculated for the resonant frequency and quality factor. This is mainly due to the fact that the air gap can be modeled as a capacitor $C_{ag}$ in series with the coupling capacitor $C_c$ of Figure 1(d), which significantly contributes to an increase in the resonant frequency of the proposed sensor. The increases in resonant frequency for rotor1 and rotor2 with a 100 µm air gap was found to be 477 MHz and 171 MHz respectively, which is greater than the detectable angular rotational bandwidths at $\Delta f$ = 125 MHz and 42 MHz (see Figure 6(a)). However, it can be seen from the circuit model in Figure 1(d) and the relation of *S*-parameters in (2) and (3) that the presence of $C_{ag}$ does not strongly affect the phase relation between the reflection coefficients of the proposed two-port sensor. To quantitatively compare the maximum error in the three measurable parameters due to the air gap, the error in relative phase, the error in resonant frequency, and the error in the quality factor for rotor2 have all been calculated and are given in Table III. It can be observed from this table that the proposed scheme shows much higher tolerance to the air gap between the stator and the rotor than do other measurement scenarios involving the resonant frequency or *Q*-factor.

TABLE III. MAXIMUM ERROR IN MEASUREMENT OF VARIOUS PARAMETERS WITH CONSIDERATION OF AIR GAP

| Parameters | Max. error for air gap (Δz = 100 µm) | | | Dynamic Range | Max. % Error |
|---|---|---|---|---|---|
| | $\theta$ = -90° | $\theta$ = 0° | $\theta$ = 90° | | |
| $\phi$ (degree) | -10.9 | 0.9 | 10.8 | ± 269 | ± 4.1 |
| $f_r$ (MHz) | 167 | 171 | 164 | 42 | 407 |
| $Q$ | 19 | 10 | 21 | 74 | 28.4 |

## V. MEASUREMENT AND RESULTS

The planar microwave sensor, consisting of one stator on 0.5-mm-thick RT5880 laminate and three rotors—rotor A [1.5-mm-thick RT5880 laminate ($\varepsilon_r$ = 2.2, $tan\delta_r$ = 0.009)], rotor B [1-mm-thick FR4 laminate ($\varepsilon_r$ = 4.3, $tan\delta_r$ = 0.025)], and rotor C (0.5-mm-thick RT5880 laminate)—was fabricated using the standard photolithography techniques. Two subminiature versions A (SMA) female type connectors were mounted on the stator to provide a proper connection with a vector network analyzer (VNA) using a set of coaxial cables. Bottom and top views of the fabricated stator are provided in Figure 11(a) and (b), while photographs of rotors A, B, and C are given in Figure 11(c), illustrating angular rotations of -90°, 0°, and 90°. To validate the scheme and to minimize the error caused by manual handling of the prototype, movement was restricted to angular rotation. To this end, a support fixture made of acrylonitrile butadiene styrene (ABS) was made using 3D printing technology. The jig holds the stator and rotor components in perfect alignment while allowing for controlled angular rotation around the axis by means of a circular knob with a printed angle scale in degrees. The fabricated sensor was carefully mounted on the jig and connected to a VNA (an Agilent Technologies N5242A PNA-X network analyzer, 10 MHz–26.5 GHz). A photograph of the measurement setup is shown in Figure 11(d). A close view of the stator and rotor assembly is also provided in the inset to Figure 11(d), where it can be seen that the rotor and stator are perfectly aligned with the help of a metal bar attached to the circular knob. It can also be noted here that the metal bar and rotor are isolated with the help of 5-mm-thick ABS plastic (of dielectric constant 3.2 and loss tangent 0.02) and 5-mm-thick Rohacell foam (with dielectric constant 1.07 and loss tangent 0.002). The Rohacell foam glued to the rotor gives two advantages: it provides suitable mechanical strength for the angular rotation and it creates an air-like-medium for good isolation from ABS and metal on the top assembly.

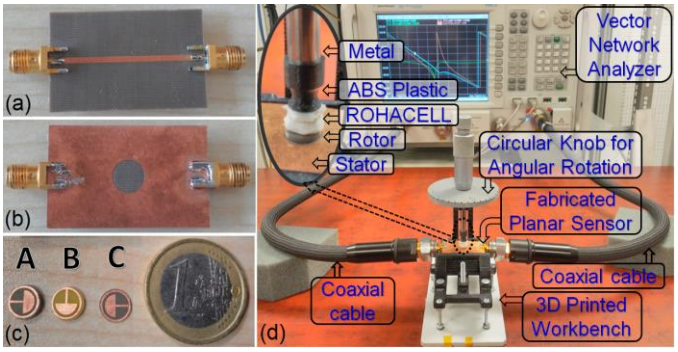


Figure 11. (*a*) Bottom and (*b*) top views of fabricated stator, (*c*) rotor A (1.5-mm-thick RT5880 laminate), rotor B (1-mm-thick FR4 laminate)c and rotor C (0.5-mm-thick RT5880 laminate), and (*d*) measurement setup for directional angular rotation.

MOST WIEDZY Downloaded from mostwiedzy.pl

Before the measurement, the VNA was calibrated using an electronic calibration module (N4691-60004: 300 kHz–26.5 GHz) provided by Agilent Technologies. Two-port calibration was performed on 1601 equispaced frequency points between the start and the stop frequencies of 3 GHz and 7 GHz, respectively, with an intermediate frequency bandwidth (IFBW) of 500 Hz. The magnitude and phase response of the measured two-port S-parameters corresponding to each of the rotors at $\theta$ = -90°, 0° and 90° are provided in Figure 12. Figure 12 allows us to see that the magnitude response is indeed quite incapable of providing information on the sense of angular rotation of the rotors, while it is possible to detect and measure the angular direction and rotation of the rotors using the phase of the reflection coefficients.

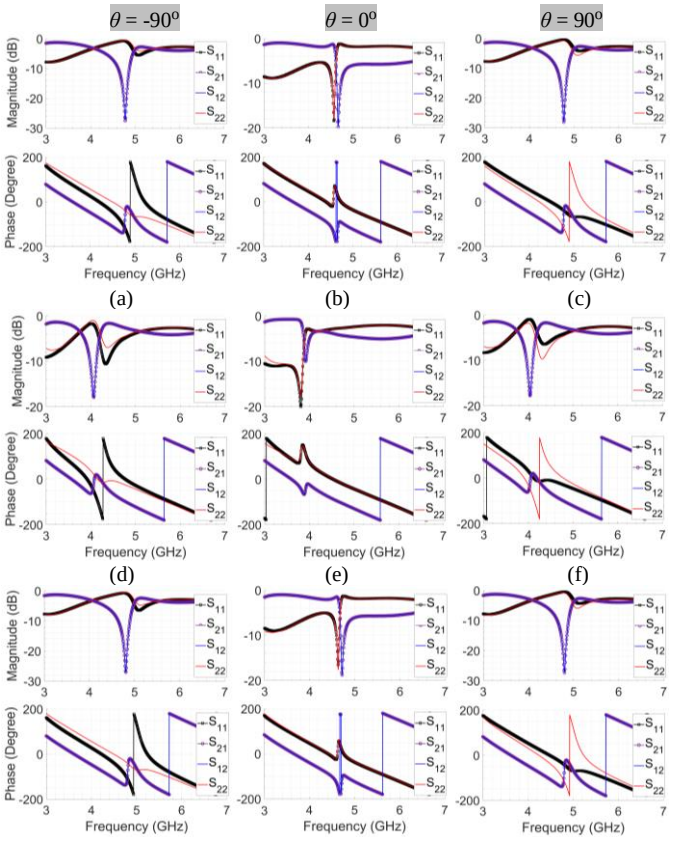


Figure 12. Magnitude and phase response of two-port S-parameters of the fabricated sensor with rotor A at $\theta$ = (*a*) -90º, (*b*) 0º, and (*c*) 90º; with rotor B at $\theta$ = (*d*) -90º, (*e*) 0º, and (*f*) 90º; with rotor C at $\theta$ = (*g*) -90º, (*h*) 0º, and (*i*) 90º, respectively.

Figure 12(a)–(c), (d)–(f), and (g)–(i) represent the two-port S-parameters of the fabricated sensor with rotor A, rotor B, and rotor C, respectively. From Figure 12 (a)–(c), it can be observed that the stator with 1.5-mm-thick rotor made from RT5880 laminate has a resonant frequency of 4.665 GHz and a quality factor of 169 at $\theta$ = 0°, while an average bandwidth of 106 MHz was recorded for an angular rotation in either the anticlockwise or clockwise direction. From Figure 12 (d)–(f), it can be seen that the stator with the 1-mm-thick rotor from FR4 laminate provides a resonant frequency of 3.95 GHz and a quality factor of 51 at $\theta$ = 0°, and an average bandwidth of 96 MHz is recorded for an angular rotation in either the anticlockwise or clockwise direction. Figure 12 (g)–(i) demonstrates that the stator with the 0.5-mm-thick rotor made from RT5880 laminate has a resonant frequency of 4.715 GHz and a quality factor of 172 at $\theta$ = 0°, while the average bandwidth of 116 MHz is recorded for an angular rotation in either an anticlockwise or clockwise direction. It can be concluded from Figure 12 that the choice of the independent rotor gives the freedom to select the operating frequency band.

Rotors A, B, and C were placed on the stator in turn, and the two-port S-parameters were carefully measured while manually rotating the rotor at successive steps of 10° from -90° to 90°. The relative phase $\phi$ was calculated from each set of measured data in the wide frequency band from 3 GHz to 7 GHz; the results are plotted in Figure 13. Figure 13 (a), (b), and (c) presents the variation in $\phi$ with respect to the wideband frequency for rotors A, B, and C, respectively. In these figures, a narrowband region of frequency is highlighted where the transmission zero is observed for each angular rotation. From Figure 13, we can see that the direction of angular rotation is easily distinguishable by looking at the sign of $\phi$, with clockwise rotation giving positive values and anticlockwise rotation negative values. The value of the clockwise or anticlockwise angle of rotation increases by traversing the curves of $\phi$ from left to right, as depicted by the arrow in Figure 13.

Each measurement was repeated at least six times, and the mean value is plotted in Figure 14; the maximum deviation in measurement is shown by the error bars. To compare the measurement with the data obtained from full-wave FEM code by imitating the actual measurement situation (that is, the stator with SMA connectors and the rotor connected to the axis of the circular knob using 5-mm-thick polymethacrylimide (PMI) structural foam) are also plotted in Figure 14, from which we can see that the measurements are in good agreement with the numerical data. The maximum and minimum sensitivity for rotors A, B, and C from the measurements were 3.2 (°/°), 3.1 (°/°); 2.9 (°/°), 2.8 (°/°); and 3.1 (°/°), 2.8 (°/°), respectively. We note that the sensitivity of rotors A and C is calculated for the angular span of ± 10° to ± 90°, while for rotor B it was calculated for ± 20° to ± 90°.

From Figure 14(a) and (b), we can observe that the measured curves of rotor A and rotor C closely follow the simulated curve, and that the overall response is in agreement with the theoretical and numerical explanation provided in Figure 7. However, even though the measured response of rotor B in the angular span -20° < $\theta$ < 20° was found to be in good agreement with the simulated response of rotor with the FR4 (lossy) substrate, the overall response in this angular region is quite different from that for rotors A and B. To attempt to explain this different behavior, we computed the response of rotor B, neglecting the loss in FR4 in the numerical simulations. This result is given in Figure 14(b): it shows that, neglecting loss in FR4, the relation of the relative phase with angular rotation in -20° < $\theta$ < 20° is similar to the measured and simulated responses of the other two rotors that use the low-loss material. Figure 14 allows it to be concluded that the derivation and discussion of change in the relative phase with respect to the angular rotation of rotors in this paper is mainly applicable to rotors with lossless or very low-loss dielectric materials.

MOST WIEDZY Downloaded from mostwiedzy.pl

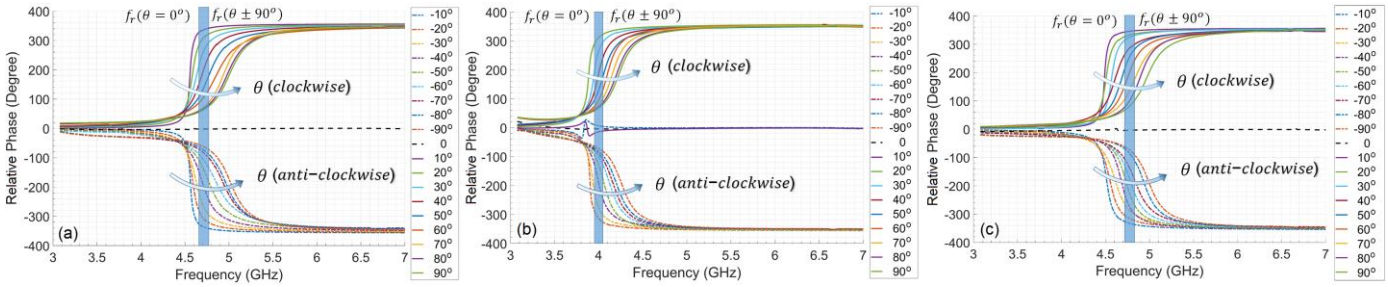


Figure 13. Calculated relative phase from measured two-port reflection coefficients of the fabricated sensor for (a) rotor A, (b) rotor B, and (c) rotor C.

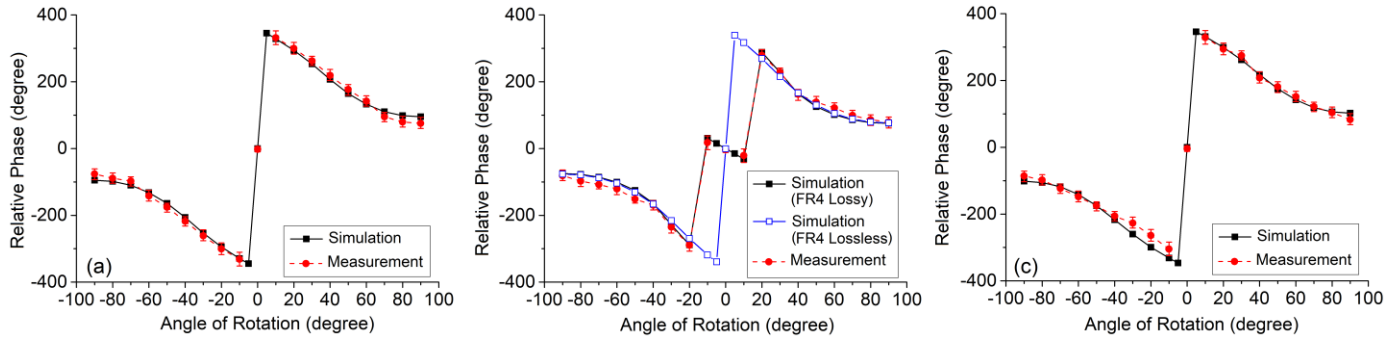


Figure 14. Comparison of the measured and simulated response of relative phase for the fabricated sensor for (a) rotor A, (b) rotor B and (c) rotor C.

To demonstrate the novelty of the proposed approach, the state of the art of rotation sensors is presented in Table IV, where the advantages of the proposed sensor can be clearly identified.

TABLE IV. STATE OF THE ART OF ANGULAR DISPLACEMENT SENSORS

| Ref. | Type of Stator: Rotor | Dynamic Range | Sensitivity | Selection of operating frequency | Direction of Rotation |
|---|---|---|---|---|---|
| [6] | CPW: SRR | 0° to 90° | 0.26 dB/° | X | X |
| [7] | CPW: S-SRR | --- | --- | X | X |
| [9] | Microstrip: U-type | 0° to 180° | 1.81 MHz/° | X | X |
| [10] | CPW: Horn-type | 0° to 8° | 1.75 dB/° | X | X |
| This work | Microstrip: MCSRR with RT5880 and FR4 | -90° to 90° | Min.: 2.8 °/° Max.: 3.2 °/° | ✓ | ✓ |

## VI. CONCLUSION

A new planar microwave sensor capable of measuring of the direction of angular rotation has been proposed, designed, fabricated, and tested. This sensor is based on a modified complementary split-ring resonator (MCSRR) coiled to a microstrip line, and uses relative phase measurements. This new scheme has been found to be tolerant of positioning error and the presence of an air gap between the stator and the rotor. The proposed planar sensor gives flexibility in selecting the operating frequency, and has improved sensitivity in angular rotation, high resolution in detecting the angular direction from the initial position, and a wide dynamic range of measurement. It is low in cost, small in size, light in weight, and can be implemented with a monolithic microwave integrated circuit (MMIC).

## REFERENCES


[1] L. Young and A. J. Bahr, "Proposal for a microwave rotation sensor," *Proceedings of the IEEE*, vol. 56, no. 11, pp. 2076–2077, Nov. 1968.

[2] A. E. Saunders and D. D. Stancil, "Magnetostatic wave ring resonator with a rotating thin film," *IEEE Trans. Magn.*, vol. 24, no. 6, pp. 2805–2807, Nov. 1988.

[3] Z. Wu, L. Bian, J. Zhang and X. Wang, "Magnetoelectric effect for rotational parameters detection," *IEEE Trans. Magn.*, vol. 52, no. 7, pp. 1–4, July 2016.

[4] S. R. Khan and M. P. Y. Desmulliez, "Implementation of a dual wireless power transfer and rotation monitoring system for prosthetic hands," *IEEE Access*, vol. 7, pp. 107616–107625, 2019.

[5] V. Sipal, A. Z. Narbudowicz and M. J. Ammann, "Contactless measurement of angular velocity using circularly polarized antennas," *IEEE Sensors J.*, vol. 15, no. 6, pp. 3459–3466, June 2015.

[6] J. Naqui and F. Martín, "Transmission lines loaded with bisymmetric resonators and their application to angular displacement and velocity sensors," *IEEE Trans. Microw. Theory Techn.*, vol. 61, no. 12, pp. 4700–4713, Dec. 2013.

[7] J. Mata-Contreras, C. Herrojo and F. Martín, "Application of split ring resonator (SRR) loaded transmission lines to the design of angular displacement and velocity sensors for space applications," *IEEE Trans. Microw. Theory Techn.*, vol. 65, no. 11, pp. 4450–4460, Nov. 2017.

[8] J. Naqui and F. Martín, "Angular displacement and velocity sensors based on Electric-LC (ELC) loaded microstrip lines," *IEEE Sensors J.*, vol. 14, no. 4, pp. 939–940, April 2014.

[9] A. Ebrahimi, W. Withayachumnankul, S. F. Al-Sarawi and D. Abbott, "Metamaterial-inspired rotation sensor with wide dynamic range," *IEEE Sensors J.*, vol. 14, no. 8, pp. 2609–2614, Aug. 2014.

[10] A. K. Horestani, D. Abbott and C. Fumeaux, "Rotation sensor based on horn-shaped split ring resonator," *IEEE Sensors J.*, vol. 13, no. 8, pp. 3014–3015, Aug. 2013.

[11] A. Maleki Gargari et al., "A wireless metamaterial-inspired passive rotation sensor with submilliradian resolution," *IEEE Sensors J.*, vol. 18, no. 11, pp. 4482–4490, June 2018.

[12] A. K. Jha, N. Delmonte, A. Lamecki, M. Mrozowski and M. Bozzi, "Design of microwave-based angular displacement sensor," *IEEE Microw. Wirel. Compon. Lett.*, vol. 29, no. 4, pp. 306–308, April 2019.


MOST WIEDZY Downloaded from mostwiedzy.pl

[13] J. Mata-Contreras, C. Herrojo and F. Martín, "Detecting the rotation direction in contactless angular velocity sensors implemented with rotors loaded with multiple chains of resonators," *IEEE Sensors J.*, vol. 18, no. 17, pp. 7055–7065, Sept. 1, 2018.

[14] J. Naqui, M. Durán-Sindreu, and F. Martín, "Modeling split ring resonator (SRR) and complementary split ring resonator (CSRR) loaded transmission lines exhibiting cross polarization effects", *IEEE Ant. Wirel. Propag. Lett.*, vol. 12, pp. 178–181, 2013.

[15] J. Bonache, M. Gil, I. Gil, J. Garcia-Garcia and F. Martin, "On the electrical characteristics of complementary metamaterial resonators," *IEEE Microw. Wirel. Compon. Lett.*, vol. 16, no. 10, pp. 543–545, Oct. 2006.

© 2020 IEEE. Personal use of this material is permitted. Permission from IEEE must be obtained for all other uses, in any current or future media, including reprinting/republishing this material for advertising or promotional purposes, creating new collective works, for resale or redistribution to servers or lists, or reuse of any copyrighted component of this work in other works.

MOST WIEDZY Downloaded from mostwiedzy.pl